Hindawi
International Journal of Aerospace Engineering
Volume 2020, Article ID 1086518, 19 pages
https://doi.org/10.1155/2020/1086518

Research Article

Advanced Design of a Full-Scale Active Morphing Droop Nose

Alessandro De Gaspari, Vittorio Cavalieri, and Sergio Ricci

Department of Aerospace Science and Technology, Politecnico di Milano, 20156 Milano, Italy

Correspondence should be addressed to Alessandro De Gaspari; alessandro.degaspari@polimi.it

Received 29 November 2019; Revised 18 May 2020; Accepted 22 May 2020; Published 18 June 2020

Academic Editor: Jacopo Serafini

This paper describes the design of a morphing droop nose conceived to increase the performance in high-lift conditions of a twin-prop regional aircraft, while ensuring the natural flow laminarity of the wing. Starting from the results obtained in a previous phase, mainly concerned with the performance augmentation, a detailed structural design is conducted. The main aim is the achievement of a feasible solution based on the use of conventional materials, such as aluminium alloy for the internal structure and glass-fibre for the skin. A finite element model of the complete device is generated for the three-dimensional shape quality evaluation and for the skin structural verification. Stress analyses on high-fidelity models of the single adaptive ribs are also performed. At the same time, various design aspects are evaluated, such as installation and inspection issues, actuation power, and weight considerations. All these requirements contribute to the definition of an advanced and complete solution for the device, up to the realization of a detailed CAD model. Final verification on the virtual prototype assesses the functionality of the device when attached to the wing-box. Moreover, the bird impact safety of the leading edge is demonstrated according to the certification rules.

1. Introduction

In the framework of Clean Sky 2 REG–IADP AIRGREEN 2 (AG2) project, many morphing concepts are analysed to be applied to a next-generation twin-prop regional transport aircraft. One of the developed devices is a morphing Droop Nose whose aim is to achieve the requested high-lift performance during take-off and landing and, at the same time, to preserve the optimal Natural Laminar Flow (NLF) wing shape in cruise.

The adoption of the morphing leading-edge device can ensure the desired high-lift performance, along with enhanced efficiency with respect to the baseline configuration, also considering that usually regional aircraft do not employ conventional slats.

From the aerodynamic perspective, the design objective is the definition of the optimal drop law and shape for the achievement of the required performance. The major challenge is the design of a structure able to guarantee the expected target shape, while satisfying the certification rules. Indeed, the design of morphing structures is a tough challenge due to the contemporary presence of conflicting requirements [1], such as a sufficient flexibility required to accomplish the shape change coupled with the typical load-bearing capability. The approach here proposed for the design of this kind of morphing device is based on an internal compliant structure connected to a flexible composite material skin.

In the last ten years, PoliMi has been involved in several projects, through which the authors have acquired an important background in the design techniques for morphing structures application [2–4]. The developed design procedure is mainly based on a multilevel multidisciplinary optimization loop [5]. At the first stage, an aerodynamic optimization with structural constraints is performed for the definition of the optimal target shape according to the requirements. Later, a multiobjective optimization analysis is used to find an internal structure based on the distributed compliance concept [6]; the stiffness is efficiently distributed so that, once actuated, the deformation of the structure produces the target aerodynamic shape. After that, additional optimization tools are used, and further considerations are included in the design process to increase the level of detail of the final solution.

The results of the design process for the considered droop nose device were preliminarily presented in [7]. In this paper, the virtual prototype is finalized, including several technological aspects, with the aim of increasing the Technology Readiness Level (TRL) of the proposed morphing device. From the structural perspective, a special effort is devoted to the selection of the skin material in order to achieve a smooth morphing surface. Regarding the internal structure, it must be found a feasible solution able to withstand the external loads without significant deformation and within the strength limits of the adopted material. The last point is especially critical since the large requested deployment of the device causes high stresses in the structure, as already seen in previous works; hence, particular attention must be given to the satisfaction of the stress limits. Actuation time and power must be analysed to check if they agree with the initial requirements. In addition, the selected actuators must be compatible with the available space. Weight evaluation is also essential, in order to estimate if overall the complete device made of structure, actuation, and connections can guarantee the expected augmented performances that have been computed by the initial aerodynamic analyses. The proposed device must satisfy some other requirements related to its assembly on the aircraft and the possibility to carry out scheduled inspection easily. Moreover, due to the flexibility of the leading-edge skin, the structure itself is not able to pass bird impact test; hence, an appropriate support structure is required; also in this case, the conceived solution must fit in the available space. Final verification includes the analysis of the mutual interaction between the wing-box deformation and the droop nose deployment.

This paper is organized as follows. Section 2 describes the requirements for the droop nose device and its layout, the adopted design procedure and the resulting configuration. Section 3 addresses the refined structural design of the device, while Section 4 reports the stress verification. Section 5 illustrates various features of the selected technology solution, such as the type of actuation, its installation and the required power, but also weight considerations, assembly and inspection issues. Then, Section 6 discusses the verification in terms of droop nose/wing-box interaction and bird impact protection. Finally, Section 7 draws the conclusions of the entire work.

2. Morphing Droop Nose

The considered leading-edge morphing device is designed to be installed on 90 passengers, twin prop Regional Aircraft, that is one of the reference aircraft for the Regional-IADP platform, in the framework of the Clean Sky 2 AIRGREEN project. Table 1 reports the main characteristics of the reference aircraft.

According to the wing layout, the morphing Leading Edge is composed by an inboard region, which extends from the wing root to the nacelle, and an outboard region, which continues after the nacelle up to the wing tip. The chordwise extension of the device is defined by considering the front spar position at the 16% of the local chord.

Table 1: Reference aircraft characteristics.

Maximum take-off weight	32560 kg
Maximum zero fuel weight	31200 kg
Cruise Mach at 20000 ft	0.52
Landing Mach at sea level	0.197
Mean aerodynamic chord	2.565 m
Reference wing area	32.384 m^2
Reference wing span	14.827 m

2.1. Initial Design Requirements. The main objective of the morphing droop nose is to delay the wing stall in take-off and landing conditions, enhancing the maximum lift coefficient. At the same time, the skin surface must remain smooth in order to preserve flow laminarity, moreover steps and gaps are not allowed. Regarding the maximum lift coefficient, the requested increase is of 2.4% in take-off condition and of 1.7% in landing condition with respect to the reference configuration. These values must be obtained by the combined use of the addressed leading-edge device and the trailing-edge morphing flap developed at University of Naples [8, 9].

Regarding the actuation system, electro-mechanic actuation (EMA) must be installed to execute the deployment of the device. Moreover, the actuation time from the undeformed position to the maximum deflection must be less than 20 s. Both the structure design and the actuation selection should follow the requirement of minimum weight.

The two main components of the droop nose device are a continuous deformable skin connected to 20 equally spaced compliant ribs, which constitute the internal structure conceived to produce the shape change. The connection is realized through some stiffeners that extend along the entire span, which are needed to make the skin deformation uniform in the spanwise direction. Thanks to the distributed compliance concept, the internal structure can convert the displacement of one of its points, defined as input point, into the controlled displacement of the attachment points on the skin, defined as active output points. The rib input point is connected to the end of a kinematic chain, which is moved by the rotation of the drive shaft of the actuators. The actuator is then used to achieve the morphing configuration but also to keep the leading-edge fixed in the initial configuration. In both cases, the corresponding aerodynamic loads are applied to the external surface.

The complete wing of the regional aircraft equipped with the morphing droop nose is depicted in Figure 1.

2.2. Preliminary Design. The definition of the optimal external shape is performed according to an aero-structural optimization loop [10]. The objective function of the shape optimization process aims at maximizing the droop deflection along the wingspan and, at the same time, reducing the drag coefficient. The considered flight condition is the landing configuration at 10 deg. Three identified parametric sections are used for the introduction of the morphing shape changes. Regarding the constraints, a linear deflection law in spanwise direction for the outboard region is imposed. Moreover, there are two structural constraints: the first one

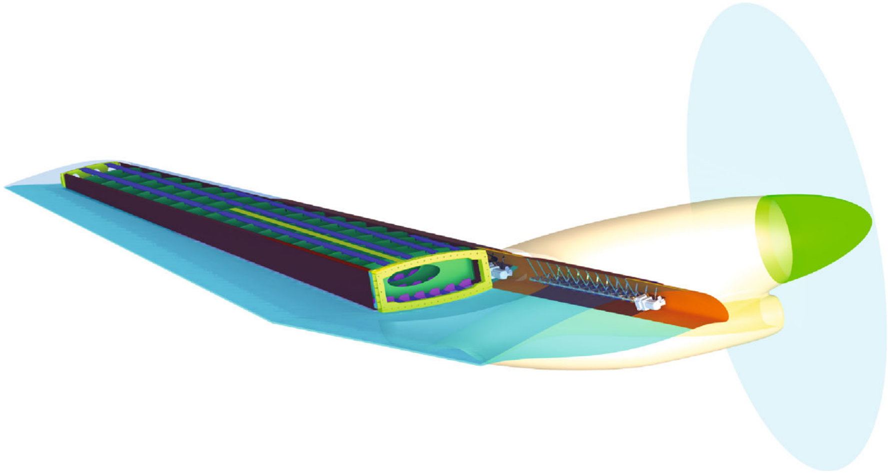

Figure 1: Twin prop regional aircraft equipped with the morphing droop nose.

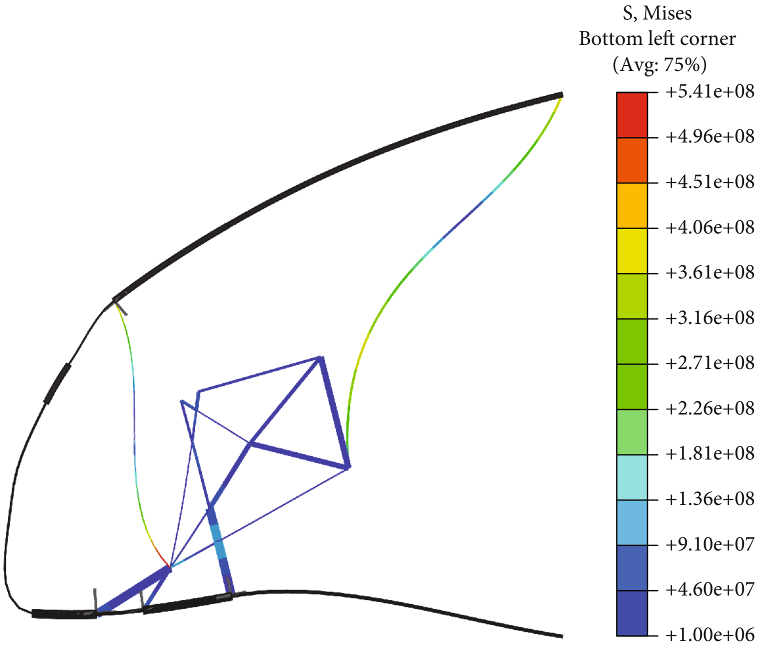

Figure 2: Topology solution for the internal structure.

is related to the skin strain, which is evaluated by geometric considerations based on the curvature change, the second one is related to the wing-box implicit constraint [10]. In particular, the allowable skin axial strain is zero, according to the constant cross-section length (CCL) concept [5], while normal strain due to bending must be limited below 1%, which corresponds to a skin maximum curvature change of 20 1/m.

The aerodynamic analyses are performed by the MSES solver, which is a fully coupled, implicit code, based on integral boundary layer (IBL) interaction [11]. The droop nose deflection is combined with the extension of a conventional trailing edge flap, which position is due to the combination of rotation and translation, and it is set to around 30 deg.

The morphing leading-edge shape obtained from shape optimization is characterized by a constant droop deflection $\delta LE = 16.2^\circ$ for the inboard region, while the linear deflection law for the outboard region goes from the abovementioned value up to $\delta LE = 10.2^\circ$ at the first section of the aileron, and then gradually vanishes. The target shape obtained for the inboard region is visible in Figure 1.

Detailed three-dimensional RANS computations for the 3D wing are performed using the Onera elsA software [12] in fully turbulent mode, assessing the enhanced aerodynamic efficiency and a significant delay of stall onset by using the morphing devices. Take-off and landing flight conditions have been analysed, and a comparison of the aircraft performances has been carried out between the configurations with and without the morphing droop nose. This device leads to a constant decrease in the drag coefficient on the entire range of lift coefficient. In take-off configuration, the effect of the droop nose on the lift curve shows a stall angle increase of 2.5°. In landing configuration, the use of the morphing droop

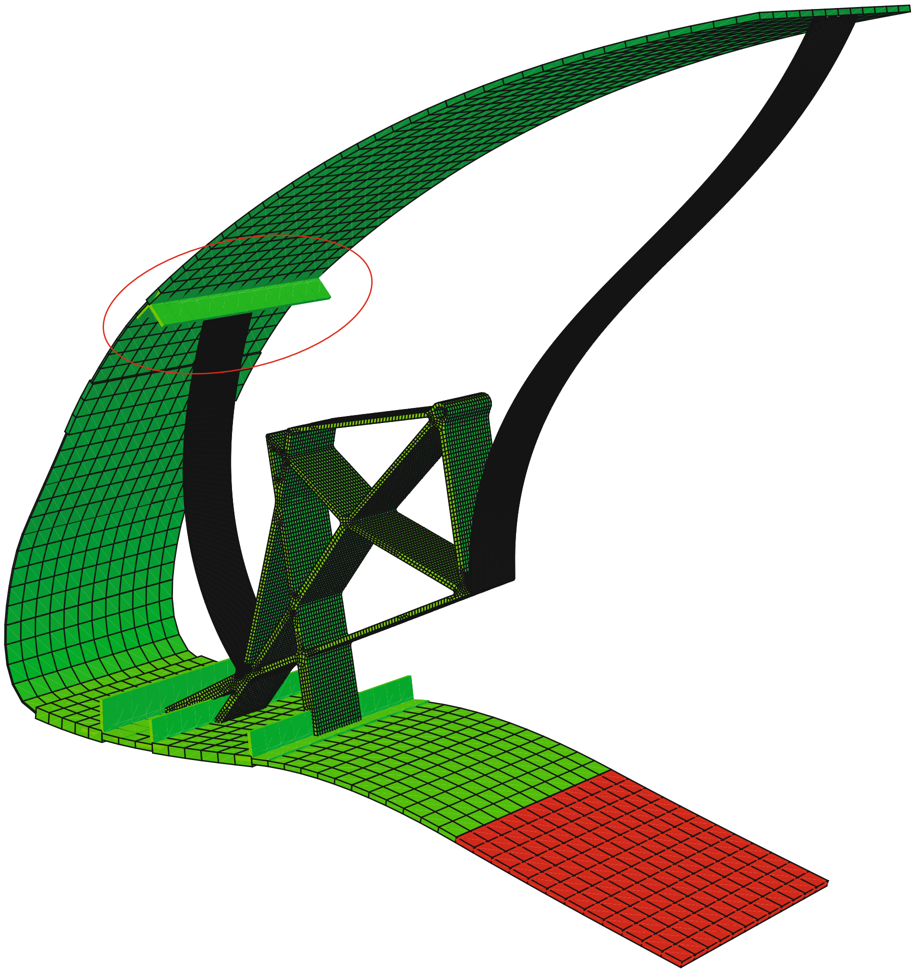

Figure 3: Finite element model of a wing section of the droop nose with the inspection panel and the new hinged connection to the top skin.

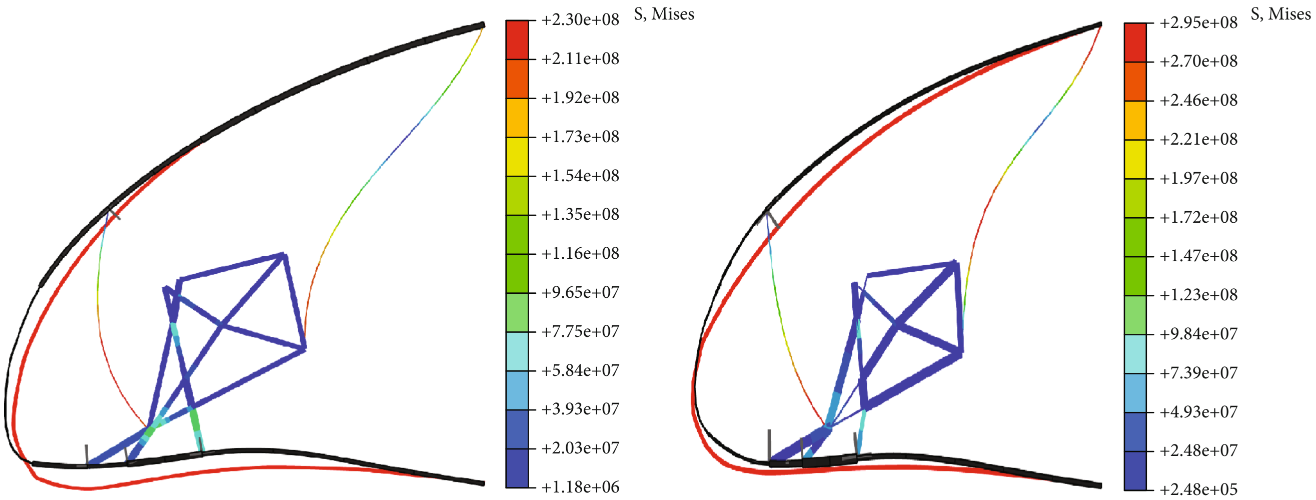

Figure 4: Inner rib (left) and outer rib (right) optimal solutions. Comparison between the optimal deformed shape and the target shape. Stress in the ribs.

nose increases the stall angle of about 5°. The droop nose is necessary for landing conditions to guarantee a maximum lift coefficient that satisfies the AG2-NLF aircraft performance [13].

After the definition of the optimal aerodynamic shape according to the requirements, a dedicated optimization process is adopted for the design of the optimal internal

Table 2: Aluminium alloy mechanical properties.

Parameter	Value
Young modulus	72000 MPa
Poisson's coefficient	0.33
Yield strength	470 MPa
Ultimate strength	540 MPa

Table 3: Glass-fibre reinforced polymer mechanical properties.

Parameter	Value
E_{11}	45700 MPa
E_{22}	13500 MPa
ν_{12}	0.27
G_{12}	5400 MPa
G_{13}	5400 MPa
G_{23}	2000 MPa
Longitudinal tensile strength	1999 MPa
Transverse tensile strength	62.0 MPa
Longitudinal compressive strength	-965 MPa
Transverse compressive strength	-155 MPa
In-plane shear strength	93.1 MPa

Table 4: Thickness distribution for the skin structural layer.

Region ID	Number of plies	Total thickness (mm)
1	14	2.8
2	26	5.2
3	16	3.2
4	6	1.2
5	2	0.4
6	2	0.4
7	6	1.2
8	4	0.8
9	12	2.4
10	12	2.4

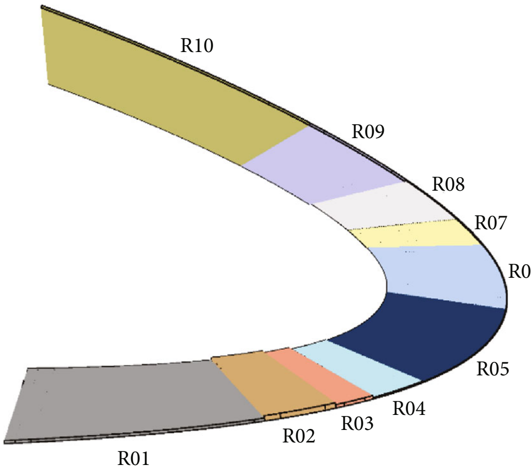

Figure 5: Skin partition and region identifiers.

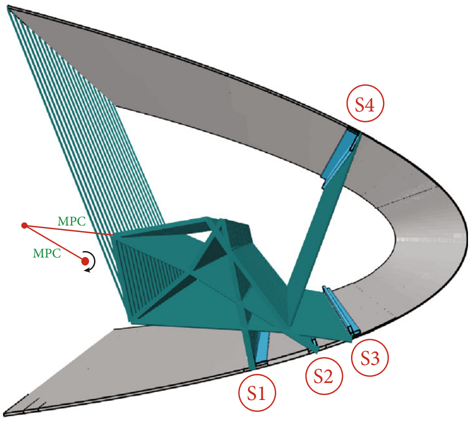

Figure 6: Complete finite element model of the droop nose.

compliant structure that enables, once actuated, to achieve the optimal target previously defined. This design stage is based on a multiobjective genetic algorithm coupled with a load-path representation and an in-house finite volume beam model solver [2, 5]. This multiobjective approach, incorporated into an elitist nondominated sorting genetic algorithm (NSGA–II) [14], is suitable to deal with the conflicting requirements of external shape change and load-carrying capability. Indeed, different objective functions are considered and simultaneously minimized by the algorithm, namely: (i) the least-square error between the achieved morphing shape and the target one; (ii) the strain energy in the conventional structural configuration; (iii) the stress in the compliant ribs of the morphing configuration. The analyses for the computation of the least-square error and the stress take into account the aerodynamic loads related to the morphing configuration (landing condition). The aerodynamic loads of the conventional configuration (cruise condition) are applied in the computation of the strain energy. The minimization of this function guarantees that the nose is as stiff as possible under loads; this is a structural requirement for every aerodynamic control surface.

At the end of the optimization process, the optimum solution is selected on the resulting Pareto front.

As already explained, the internal structure consists of 20 equally spaced ribs, but the described optimization works on a single rib, considering a two-dimensional model made of beam elements for the rib and the skin. The skin is clamped in correspondence of the front spar, and the actuation force is applied at the input point of the rib when the device is actuated, while this point is locked when the device is kept fixed. The result of the optimization for the root rib is the topology solution that represents the starting point of the whole structural design process [7]. Figure 2 shows the topology solution in the morphing configuration of the device.

This topology solution found during the preliminary design shows some critical points. First, the internal structure conceived to morph the shape of the skin is subject to very high stresses up to 541 MPa, which are not compatible with the strength of conventional aluminium alloys typically adopted in the aeronautical field. The appearance of such

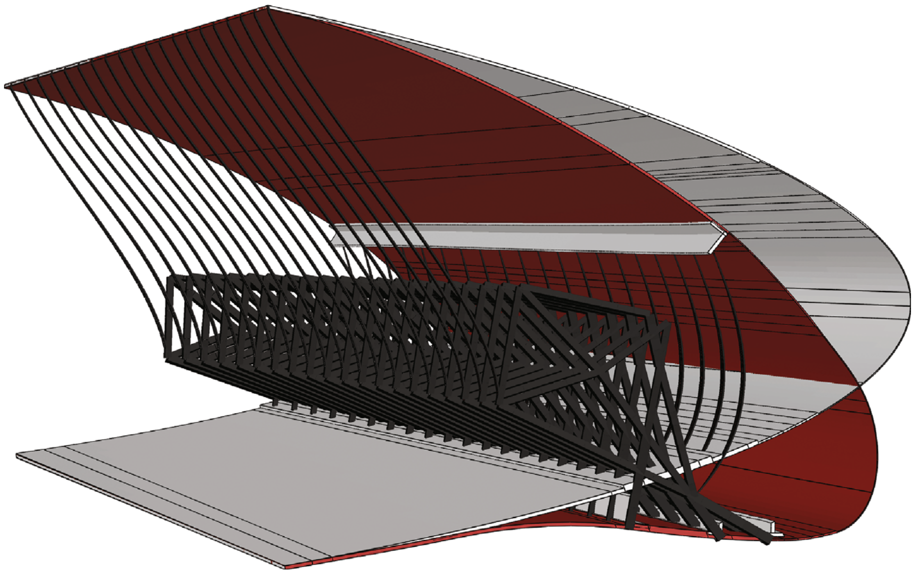

Figure 7: Three-dimensional deformed shape of the deployed droop nose.

high level of stress is due to the need to reach the requested deployment angle with the limited local chord extension of the leading-edge device. Another issue is related to the necessity to have an inspection panel for accessibility purpose, in order to lead the maintenance of the actuators. Both these aspects are treated in the subsequent detailed design of the internal structure.

Another important matter regards the spanwise extension of the droop nose. Indeed, since the outboard region is tapered, it needs proper attention to guarantee a uniform deflection behaviour along the span. The adopted approach starts from the obtained solution and makes use of the optimization analysis described in the next section.

3. Design of the Internal Structure

Regarding the problem of high stresses, the adopted strategy is to turn the fully compliant solution into a hybrid one, including the presence of a hinge in place of the upper clamped connection between the ribs and the skin. The second issue is solved by adding an inspection panel on the lower skin, adjacent to the front spar. Figure 3 shows the finite element model of a droop nose section, where both the upper hinged connection and the inspection panel are visible.

Both these two modifications are included in the subsequent design process, conducted by means of other optimization analyses. A refined process is contextually performed, aimed at obtaining an improved solution that satisfies all the additional requirements, while ensuring the agreement with the same target shape found in the first design phase.

The detailed structural design phase starts from the topology solution shown in Figure 2. Medium-fidelity models, as already depicted in Figure 3, are adopted, coupling beam elements for the rib and shell elements for the skin, thus overcoming the lower fidelity modelling of the previous stage. Nonlinear finite element analyses are performed with Abaqus software [15]. The structure under analysis is a limited spanwise portion of the skin connected to a single rib. The spanwise extension of the considered model is the length of the rib pitch, selected equal to 260 mm for the 3D device. The main modification with respect to the model used in the synthesis of the compliant structure is the inclusion of the connecting hinge between one of the rib paths and the skin. By using this alteration, it has been preliminary seen the possibility to put down the stress level.

At this stage, also, the presence of the inspection panel is considered. Its existence is modelled by clamping the opening region and excluding the panel from the structural analysis. After that, a suitable support structure has to be designed to guarantee the fixing of the panel in closed position; the executive details will be shown in the phase of CAD modelling.

A dedicated optimization analysis is conducted to ensure the satisfaction of the performance requirement represented by the optimal morphing shape change, along with the structural feasibility of the solution. For this purpose, it is selected a size optimization that acts modifying the thickness distribution of the skin and the in-plane width of the load paths which constitute the internal rib. The objective of the analysis is the minimization of the least-square error (LSE) between the achieved deformed shape and the target shape. A constraint on the maximum stress ensures the structural feasibility in the morphing configuration, while a constraint on the maximum strain energy in a critical condition for the conventional configuration guarantees the withstanding of the external loads without appreciable deformation. If the stress level in the structure is too high, there is the possibility to use the minimization of the stress as an objective function, while constraining the LSE below an upper threshold. Therefore, in the size optimization tool, it is possible to exchange objective and constraint functions. The sequential use of these complementary strategies enables further improvement in the refinement of the optimal solution, from both the shape quality and the structural feasibility perspectives.

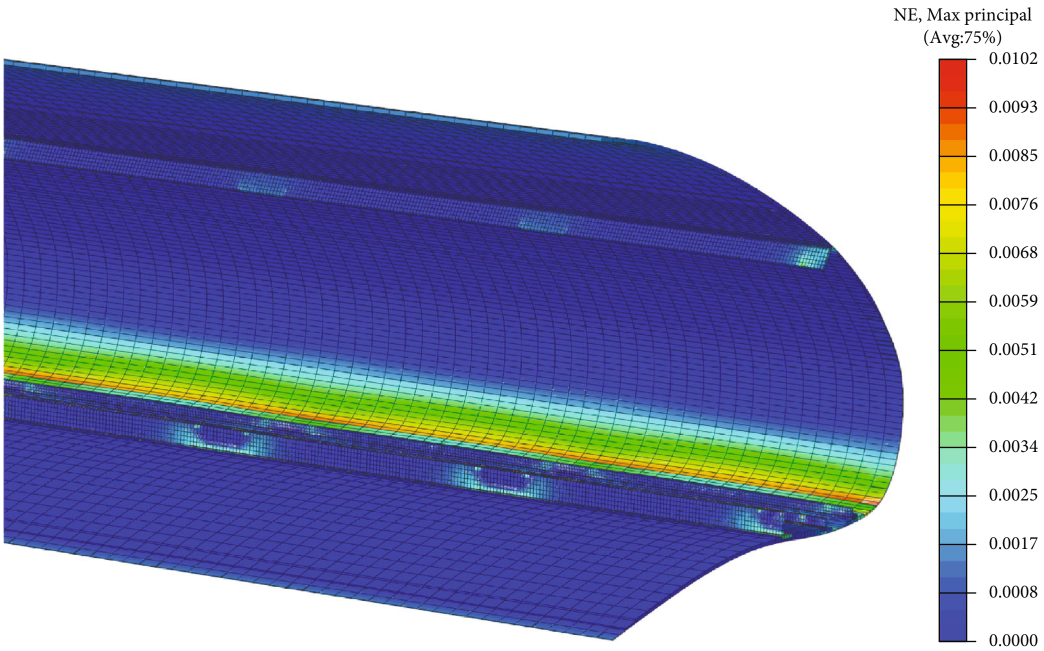

Figure 8: Maximum principal strain distribution in the skin.

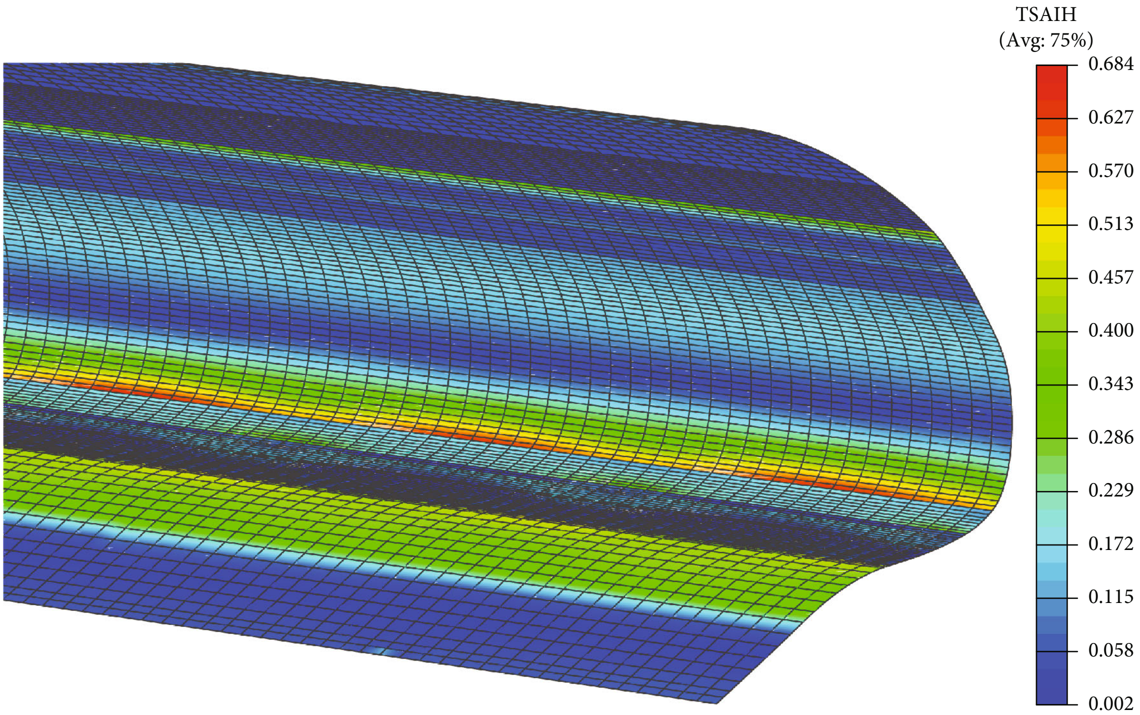

Figure 9: Strain verification for the skin: failure index distribution based on the Tsai-Hill theory.

3.1. Size Optimization Results. The size optimization procedure described before is initially applied to the compliant rib located at the wing root station. The same method is then applied to the compliant rib placed at the end of the outboard morphing region, starting from the previous solution. This approach allows to properly deal with the geometric tapering of the wing as well as the three-dimensional target shape based on a decreasing deflection law along the wingspan. The results obtained in the two cases will be then interpolated to set the cross-sectional properties of all the intermediate ribs for the complete three-dimensional model.

Figure 4 compares the optimal deformed shape and the target shape for the two cases, also showing the stress inside the ribs. Regarding the inner rib at the wing root, the obtained solution is characterized by an LSE equal to 8.7 mm, while the LSE value for the outer rib solution is

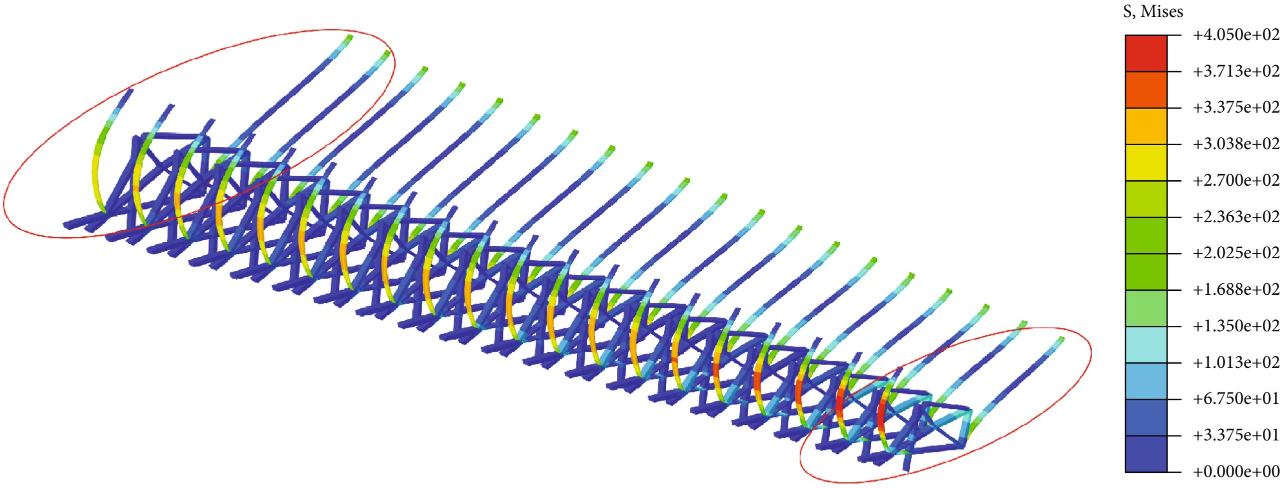

Figure 10: Stress distribution in the compliant ribs for the complete model.

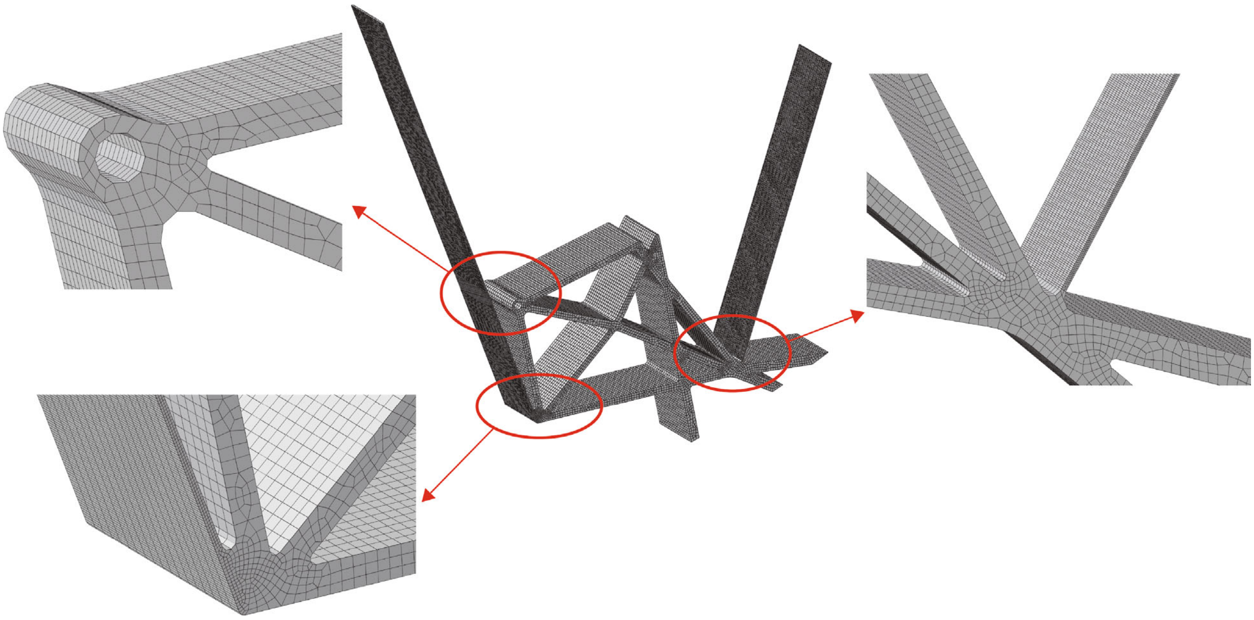

Figure 11: Detailed finite element model of a rib.

6.4 mm. The results in terms of stress reveal that stress reduction has been achieved, thanks to the adoption of the hinged connection and using the described optimization procedure, while considering at the same time the accessibility requirement related to the removable panel. On the other hand, from the shape quality perspective, the results show a worsening of the LSE values with respect to results obtained by the genetic algorithm, mainly corresponding to a lower deflection angle with respect to the desired target, but not due to a not smoothed shape.

Another work is focusing on an alternative solution for the internal structure, by the adoption of superelastic Nitinol, which is not a typical aeronautical material, but it can improve the achieved deformed shape thanks to the high recoverable strain the material is able to exhibit. This kind of material has already been applied to the design of morphing devices in [16]. However, since one of the requirements of the addressed project is the use of conventional materials, in this work aluminium alloy material is selected, with the properties reported in Table 2, and the addition of a hinged connection allows to reduce maximum stress, though not enabling better shape results. However, since the theoretical aerodynamic performance increase is higher than the request, it is possible to accept a lower deployment of the device. Anyway, the achieved deformed shape must be evaluated on the full-span model of the device, as already done in [7].

3.2. Complete Finite Element Model. Once the optimal compliant inner and outer ribs are obtained by the size optimization analysis, the sizing of all the other ribs is derived by linear interpolation of the available extreme solutions. Such ribs are modelled again using beam elements. Regarding the

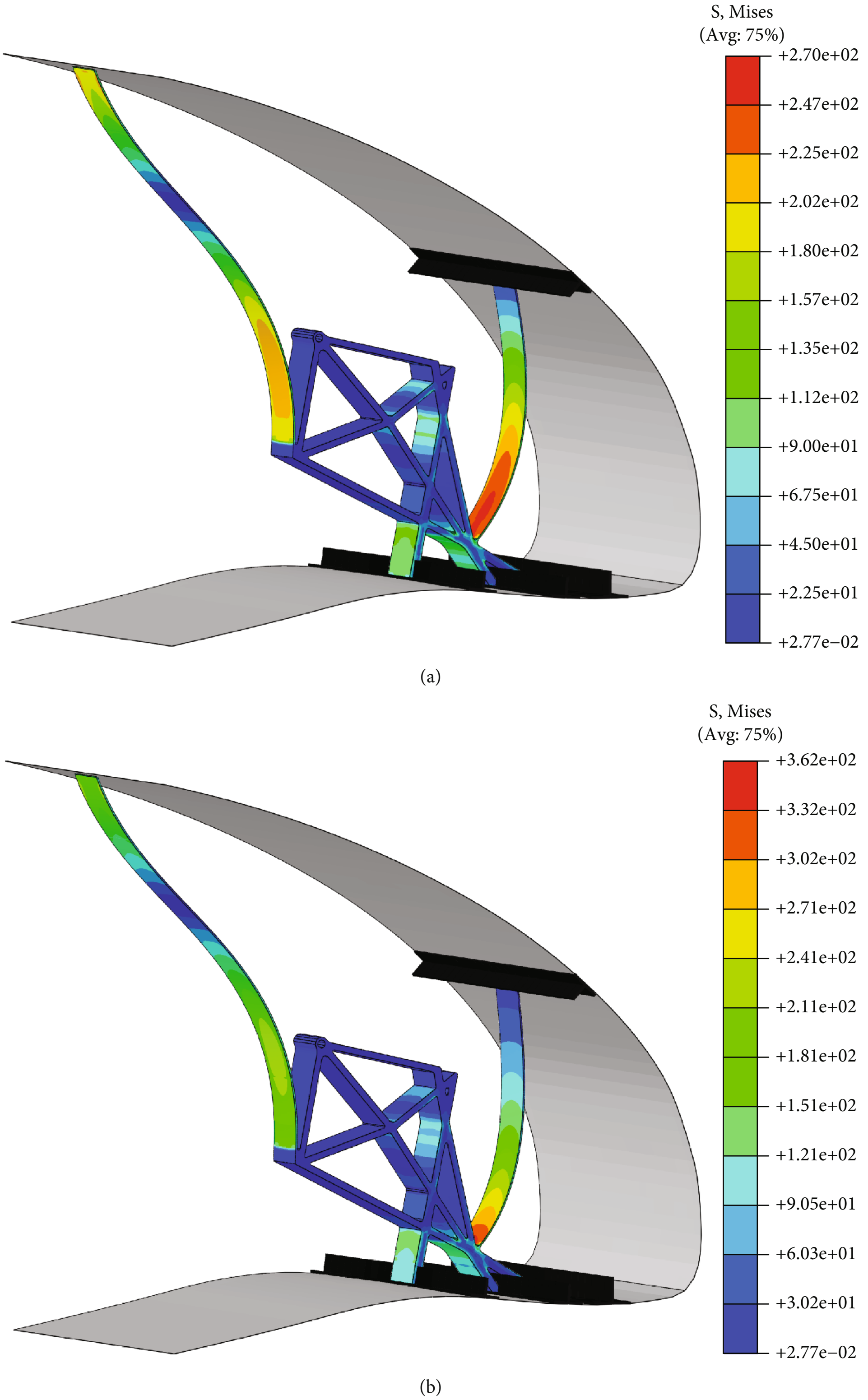

Figure 12: Stress in the root rib. (a) Limit loads. (b) Ultimate loads.

skin, it is composed by two layers: an antierosion layer made by titanium, whose thickness is equal to 0.10 mm, and a skin structural layer made by glass-fibre reinforced polymer, whose thickness distribution is determined within the described optimization analysis. Table 3 reports the material properties of the glass laminas. The thickness of each ply is 0.20 mm, and the stacking sequence of the laminate is $[0/90]_N$, where N is determined so that the total thickness of

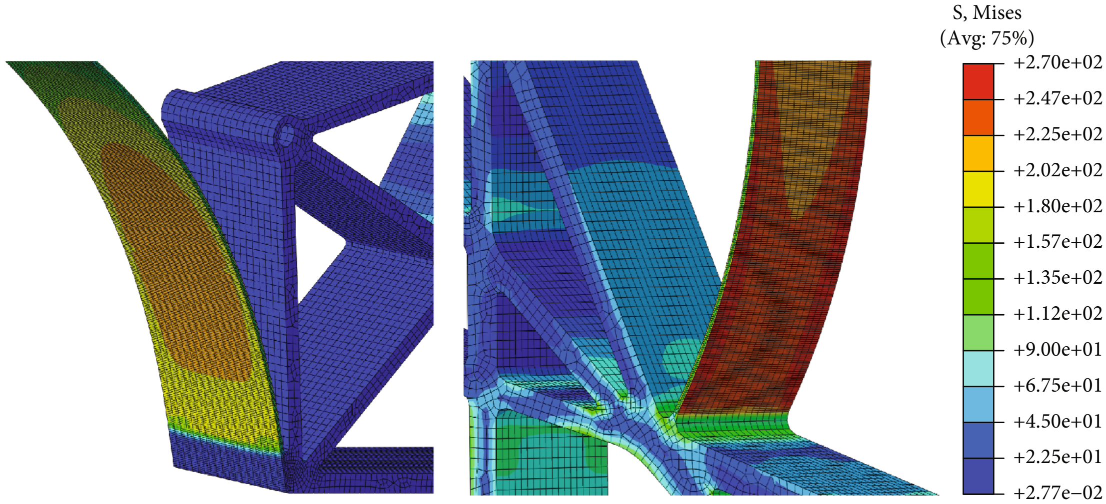

Figure 13: Root rib: detail of the most stressed regions under limit loads.

each skin region corresponds to the result of the optimization analysis, that is shown in Table 4, with reference to the region identifiers depicted in Figure 5.

The stiffeners, which are used for the connection between ribs and skin, are made of glass-fibre composite material and are supposed to be laminated together with the skin, as better explained later. Both the skin and the stiffeners are modelled using 4-node shell elements. In the complete FEM model realized in Abaqus, each rib is connected to the stringers, that are tied to the skin by means of kinematic coupling. The actuation system that introduces the morphing shape variation acting on the internal compliant structure is modelled with rigid links, and the kinematic chain is arranged through multiple point constraints (MPC). The complete model is represented in Figure 6. Overall, the model consists in 73822 elements: 67600 linear 4-nodes shells used for the skin (46306) and the stringers (21294) and 6222 linear 2-nodes beams used for the internal compliant ribs. As far as the skin is concerned, the element typical size in the high curvature region of the nose is about 5.00 mm, whereas, in the other regions, where the curvature variation is less significant, it is equal to 15.00 mm.

Static implicit nonlinear multistep analyses are performed in Abaqus, using a standard Newton solver and assuming a value of 10^{-3} as relative tolerance for convergence. The three-dimensional deformed shape achieved when the device is actuated is reported in Figure 7. It can be seen the undeformed skin region corresponding to the removable panel. The shape quality evaluation is globally successful, and the external surface remains smooth enough.

The strain distribution in the skin is shown in Figure 8. The maximum strain value of $10200\,\mu\varepsilon$ is compatible with the maximum curvature change of 1/20 m. From the same figure, it is possible to notice the strain concentration on the stringers, in correspondence with the attachment points of the ribs. Figure 9 reports the failure index distribution according to the Tsai-Hill criterion. The maximum index is 0.68; hence, the verification of the skin is successful.

Finally, the stress distribution inside the 20 compliant ribs is reported in Figure 10. The stress values are higher than the corresponding ones obtained at the end of size optimization. Further investigation is required, and it must be conducted by using more detailed finite element models. Anyway, the results from the complete model show increasing stress values from the root to the tip. For this reason, the next section focuses on the detailed verification of the ribs at the extremities.

4. Structural Verification

Starting from the optimal solutions obtained from size optimization, corresponding detailed finite element models of the extreme ribs are realized using three-dimensional solid elements. One of these models is shown in Figure 11, where the high refinement of the mesh is highlighted.

The nonlinear analyses performed on these models report high-stress concentrations with respect to the beam element models. By using a dedicated shape optimization, this issue can be overcome. Indeed, the adopted shape optimization acts on the contour surface of the internal structure redistributing the stress and decreasing the maximum peak. Final verification for the ribs, both under limit and ultimate loads, are conducted. The stress distribution in the root rib for the two cases is reported in Figure 12.

These analyses reveal acceptable safety margins, considering 470 MPa as yield strength and 540 MPa as ultimate strength. The detail of the most stressed regions in the limit loads case is shown in Figure 13.

Considering the stress values obtained by the high-fidelity analyses performed on the root rib, a safety margin SM = 0.74 for the limit loads and a safety margin SM = 0.49 for the ultimate loads are obtained.

The corresponding analyses for the rib at the tip are reported in Figure 14.

Also in this case, safety margins confirm structural feasibility. The detail of the most stressed regions in the limit loads case is shown in Figure 15.

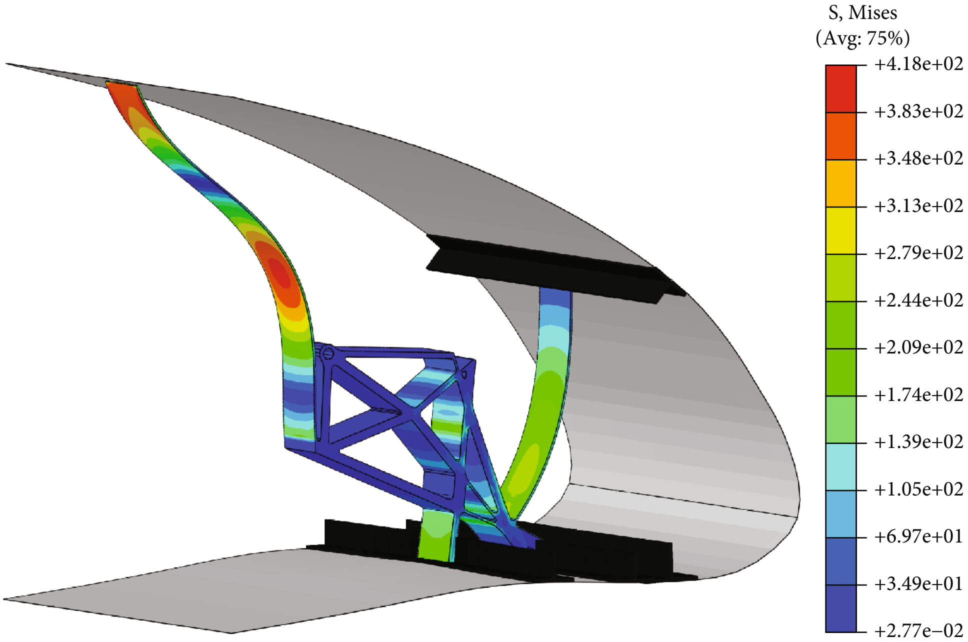

(a)

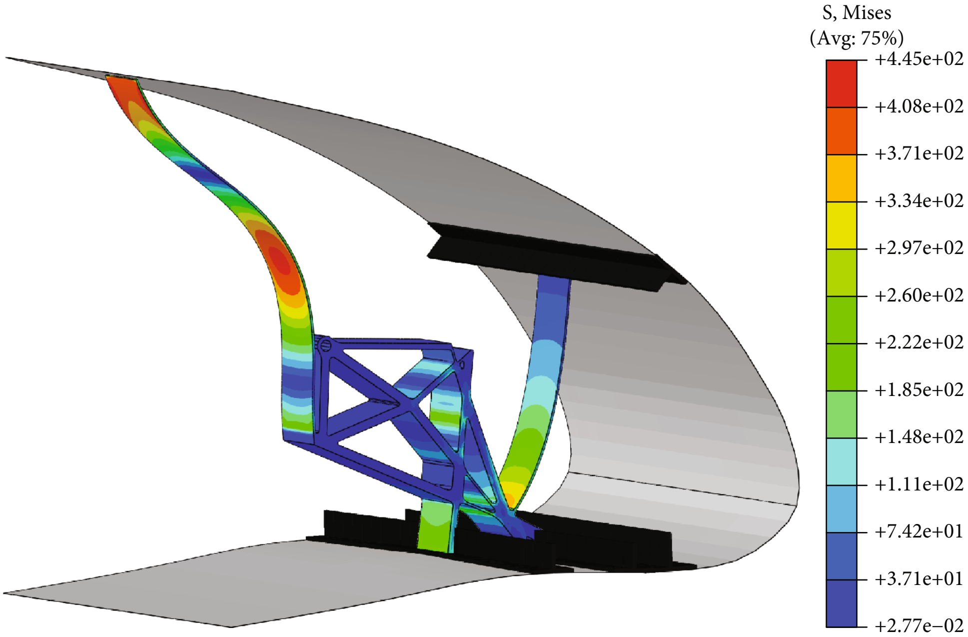

(b)

Figure 14: Stress in the tip rib. (a) Limit loads. (b) Ultimate loads.

Considering the stress values obtained by the high-fidelity analyses performed on the tip rib, a safety margin SM = 0.12 for the limit loads and a safety margin SM = 0.21 for the ultimate loads are obtained. Table 5 summarizes the safety margins in the different cases.

The described nonlinear analyses, conducted on solid element models, are more reliable than those on the corresponding beam element models. Therefore, the presented results demonstrate the structural feasibility of the proposed solution.

5. Technology Solution

Starting from the obtained solutions, corresponding CAD models for the ribs are realized. The distance from two consecutive ribs, namely the rib pitch, is equal to 260 mm. The geometry of each rib is determined by its spanwise position and the 3D shape of the wing. Regarding the in-plane thickness, the values obtained from size optimization are linearly interpolated along the span. Starting from the aerodynamic shape a 3D CAD model of the skin is also realized. The

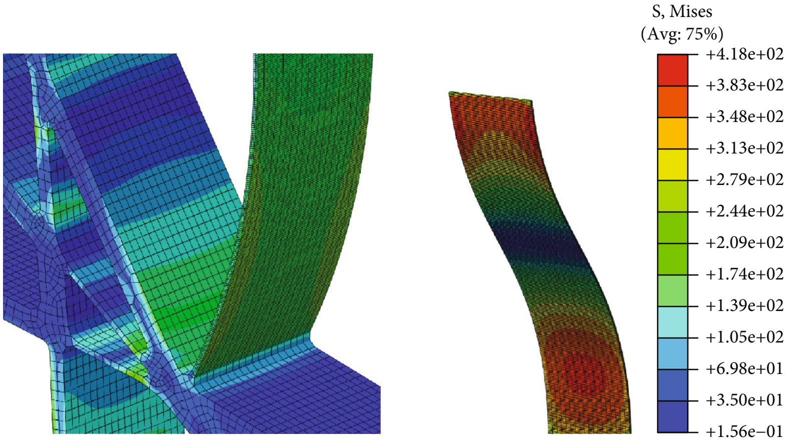

Figure 15: Tip rib: detail of the most stressed regions under limit loads.

Table 5: Safety margins for the structural verification of the ribs.

	Root rib	Tip rib
Limit loads	0.74	0.12
Ultimate loads	0.49	0.21

morphing skin is made of glass-fibre composite material, and its connection to the compliant ribs is made through the stringers. The manufacturing of the skin is intended to be performed in two halves, split at the stringer, and brought together using two curing stages. Regarding the stringers, GFRP L-shaped is used. The full integration of the stringers into the internal layers of the skin is assumed. This solution is aimed at minimizing the local stiffness in the chord direction, providing a more localized actuation of the skin. The result is the reduction of the skin local waviness. The internal ribs made of aluminium are glued to the lower stringers and are hinged to the upper stringer.

The proposed connection scheme between ribs, stringers, and skin is represented in Figure 16. In particular, the hinged connection in the upper part can be distinguished.

As already explained in the structural design section, the presence of an inspection panel is conceived on the bottom surface of the skin in order to provide access inside the droop nose as well as to be able to disassemble the device from the remainder of the structure.

In the design phase conducted by means of finite element analysis, the presence of the panel is simply introduced as a clamp constraint to model the region that is intended to remain fixed, and that does not follow the deployment of the device. Now, in the detailed CAD modelling phase, a practical solution for the realization of the panel is proposed, along with the support structure that keeps it closed in operative conditions. The inspection panel extends along the entire span of the droop nose, with a maximum chordwise length of 150 mm. Figure 17 shows a detailed view of the support structure. It consists of small rigid ribs connected to an additional stringer, which is used as bottom connection for the morphing skin and for inspection panel installation. Definitively, the skin of the morphing device is connected to the upper spar cap and to the stringer used for the inspection panel installation.

Regarding the actuation system for introducing the morphing shape variation, it consists of a kinematic chain driven by the rotation of a shaft. The relative dimension of cams and rods, and also the position of the shaft vary from the root wing section to the tip one. As shown in Figure 18, the design of the kinematic chain is performed in a parametric way, based on CAD capabilities. Indeed, rotating the shaft of 70 deg, the stroke required by the input actuation point of each compliant rib along the wingspan is achieved.

The shaft shall be able to reach every rotation angle up to the maximum one, and it shall be braked in the reached position. Therefore, thanks to the brake of the actuators, it is possible to stop the morphing device in each position, in particular the initial one and the maximum deflected one. The driveshaft is cut in two parts, and the load is distributed between them. The torque overrotation curves for the two parts are reported in Figure 19. The evaluation of the required torque considers both the stiffness of the compliant structure and the applied aerodynamic loads.

In order to meet the torque requirements, the selected actuators are two rotary actuators, installed in the fuselage and partially inside the nacelle, and one linear actuator, inside the wing-box, for the outer wing. Regarding the specifications of the rotary actuators, the motor peak torque is 11.5 Nm, there is a gearbox whose torque ratio is 60; hence, with an efficiency of 95%, it is possible to obtain a torque of 655 Nm, which is compatible with the request. The total weight of the actuators is 24 kg. The time needed to complete the total rotation is about 20 s, which is in accordance with the actuation time requirement. The detailed view of the actuators installation, compatible with the available space, is shown in Figure 20.

The connection of the actuation system to the front spar is reported in Figure 21, which also represents the first assembly step for the complete installation of the droop nose on the wing-box structure.

As better explained in the final verification section, a bird strike protection system made of some splitters is needed for such kind of morphing leading-edge device in order to satisfy

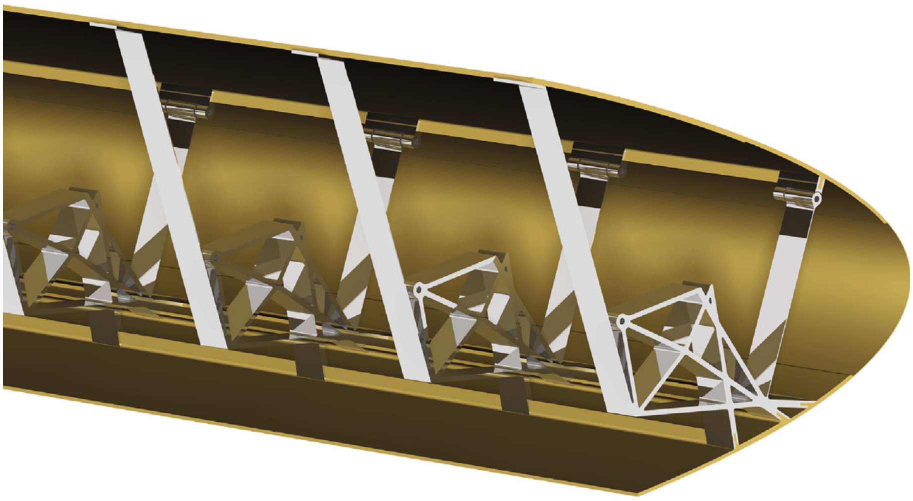

Figure 16: Detail of the assembly between the rib and the skin.

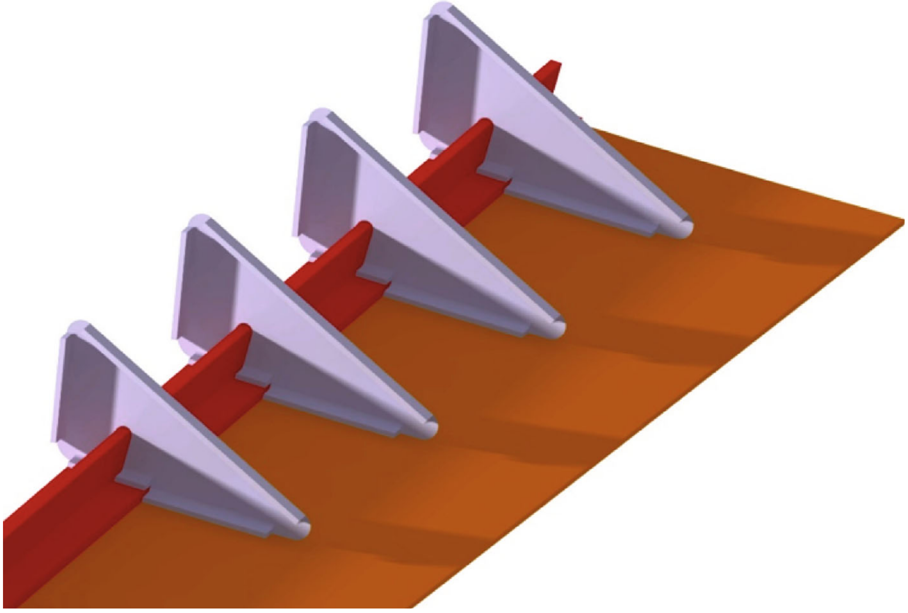

Figure 17: Support structure for the removable inspection panel.

the related certification requirements. The designed splitters are located between each pair of consecutive compliant ribs; hence, they are perfectly integrated inside the device. The second assembly step, shown in Figure 22, is the mounting of the splitters that are connected to the upper and lower spar caps. The rigid ribs for supporting the inspection panel are fixed to these splitters.

During the third step, the morphing droop nose is mounted on the wing-box connecting the skin to the upper and lower spar caps, while the compliant ribs are joined to the rods of the actuation system, working through the inspection panel. The bottom accessibility can be observed in Figure 23.

Finally, the inspection panel is mounted, and the complete wing is closed. The whole wing, made of the develop droop nose device attached to the wing-box, is depicted in Figure 24.

At the end of the modelling, some weight considerations are drawn. The weight per unit length of the morphing droop nose is 11 kg/m for the inboard region and 9.2 kg/m for the outboard region. This estimation considers the skin and the internal structure, but not the actuators. The obtained result in terms of the total weight is comparable with the typical values of leading-edge structures for aircraft of the same category, which feature values of 13 kg/m and 6.5 kg/m, with and without slat, respectively. Table 6 summarizes the maximum required torque, the weight of the actuators, and the weight per unit length of the morphing droop nose.

6. Virtual Prototype Tests

Advanced finite element simulations are performed to evaluate the interactions between the morphing droop nose and

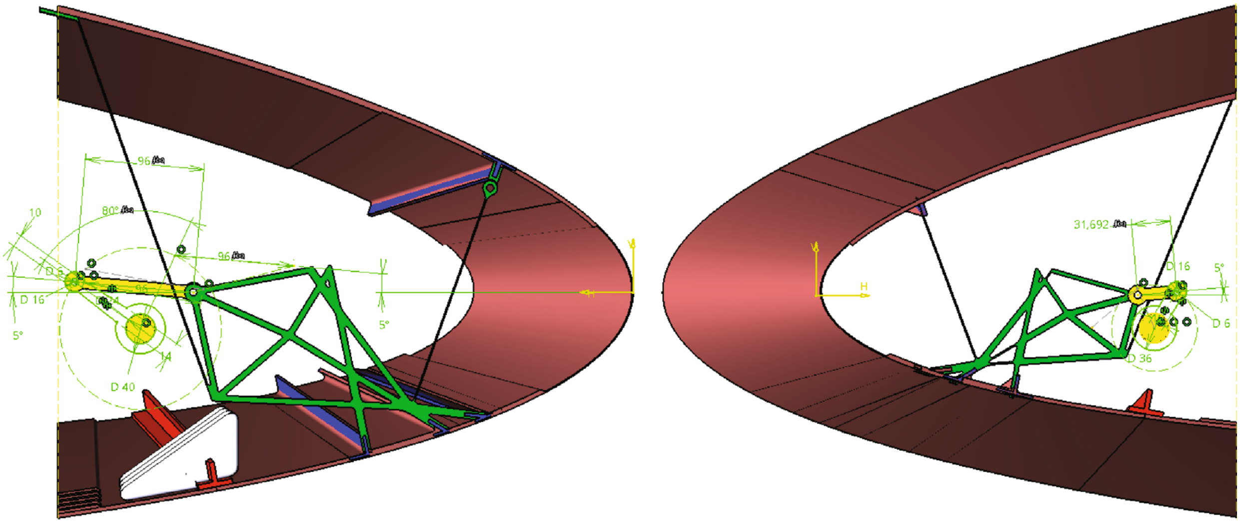

Figure 18: Parametric CAD model of the kinematic chain for the actuation system. Root section (left) and tip section (right).

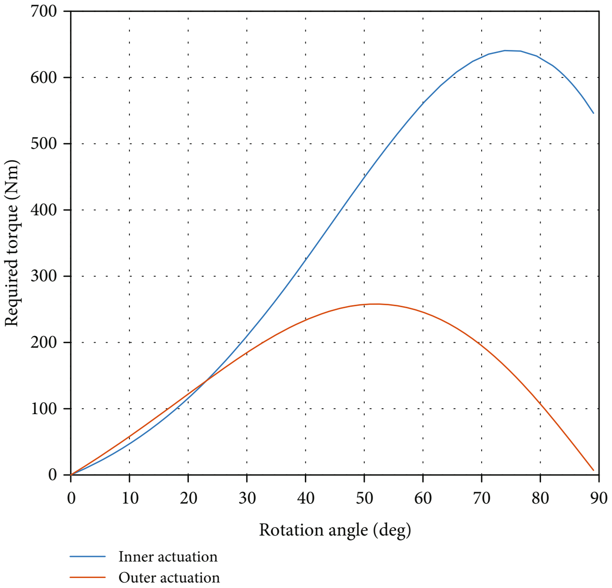

Figure 19: Required torque to achieve the requested shaft rotation.

the structural wing-box in terms of both deformability and bird strike safety requirement. This kind of analysis, on the adopted high-fidelity numerical models, is virtual prototype tests able to reproduce the corresponding experimental tests that represent the next step of the droop nose technology development.

6.1. Droop Nose/Wing-Box Interaction. A verification of the mutual interaction between the morphing droop nose device and the structural wing-box is performed. This verification is needed to evaluate the internal loads exchanged at the front spar, as well as to ensure that no undesired behaviour arises. The detailed complete model of the droop nose is attached to a representative flexible wing-box. Since a detailed FEM model of the TP90 wing-box is not available, a simplified model according the monocoque scheme has been designed, reproducing the stiffness distribution of the original wing-box.

The root section of the wing-box is clamped to the ground. The droop nose is tied to the wing-box in correspondence of the front spar, both on the upper and the lower surface of the skin. The front spar supports also the shaft, which is connected to the input points of the ribs through the kinematic chain. By applying the rotation of the shaft, the droop nose is deployed to its maximum deflection and the corresponding aerodynamic loads are applied on its external surface. Then, a vertical displacement is imposed at the tip of the wing to simulate the static deflection of the wing under aerodynamic loads. The results of this analysis, which are reported in Figure 25, show that the deformation of the wing minimally affects the behaviour of the morphing device; hence, it can still exhibit the designed functionality; in particular, it can be seen that the maximum strain increment is negligible, from 10000 $\mu\varepsilon$ to 10200 $\mu\varepsilon$.

Moreover, on the one hand, the droop nose deformation does not impact on the wing deformability; on the other hand, the wing deformation does not alter at all the cross-sectional shapes of the droop nose after the maximum morphing deflection is achieved.

6.2. Bird Strike Safety Assessment. A bird impact analysis of the final structural design is carried out to evaluate the crashworthiness capabilities of the morphing leading-edge following the regulations dictated in CS-25.631 [17]. Several numerical techniques are presented in literature to address bird impact simulation. The Lagrangian one is chosen in this work, because it offers accurate contact pressure time histories with sustainable computational efforts [18]. All the simulations are performed by means of Abaqus/Explicit code with a penalty contact formulation in order to simulate the complex interactions of the impacting body with the skin and the internal components of the investigated structure.

After a characterization of the impacting body, a numerical model used to simulate the response of the morphing leading-edge has been directly derived from the structural

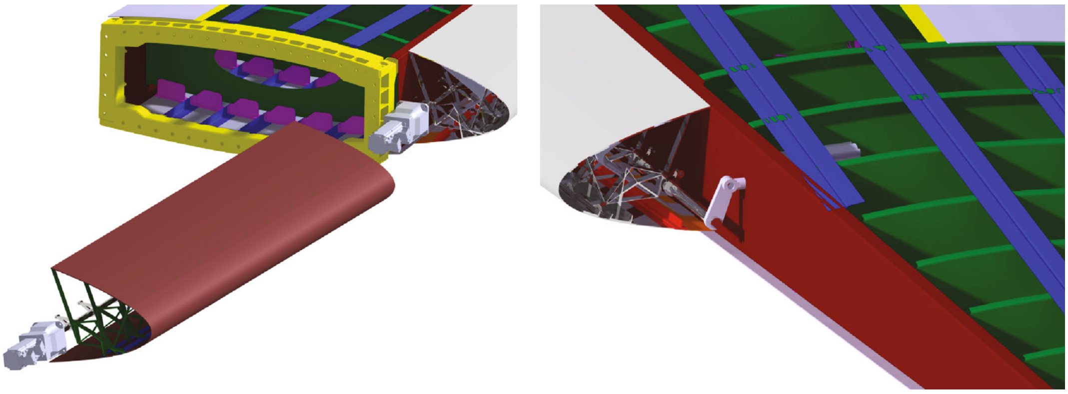

Figure 20: Installation studies for the actuators: rotary actuators (left) and linear actuator (right).

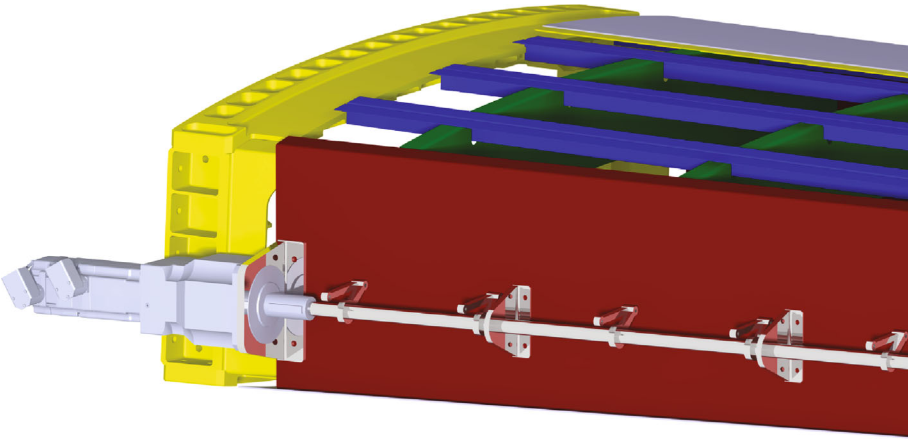

Figure 21: Connection of the actuation system to the front spar.

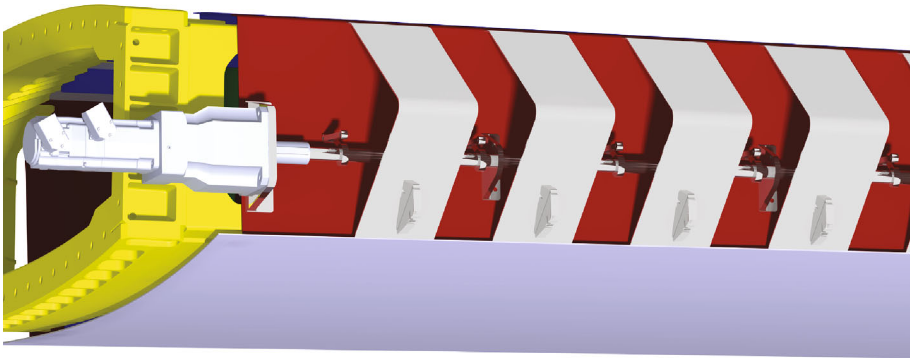

Figure 22: Assembly of the splitters on the front spar.

model previously described. Since each internal component provides an additional contribution to the crashworthiness capabilities of the structure, the entire internal mechanism has been modelled. In addition to the adaptive ribs, the actuation shaft and the deployment mechanism are also considered. A nonhomogeneous mesh, with a refinement in the central contact area, is adopted in order to maximize the accuracy without excessively affecting the computational time.

The results described here are related to the impact simulation of a bird with a mass of 1.82 kg (4 lb) and initial velocity of 142.46 m/s. The assumed velocity (relative to the bird along the aircraft flight path) is computed considering the most critical between V_C at sea-level and 0.85 V_C at 2438 m (8000 ft), according to CS-25.631 regulation. For the studied aircraft:

(i) At 2438 m, $V_C = 154.3203$ m/s (Mach = 0.4665) and 0.85 $V_C = 131.1722$ m/s

(ii) At 0 m, $V_C = 142.46$ m/s

Hence, the second one velocity is selected for the simulations.

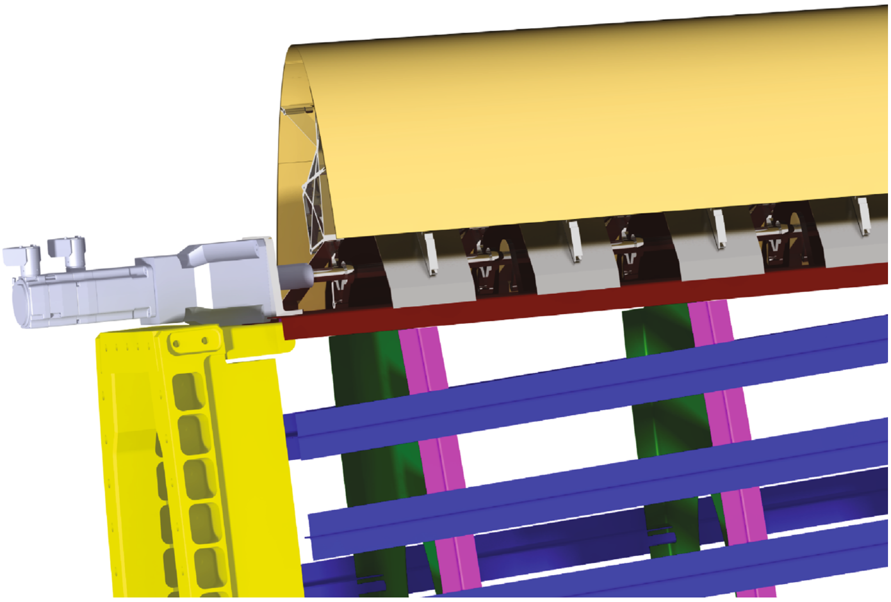

Figure 23: Assembly of the morphing droop nose and bottom accessibility.

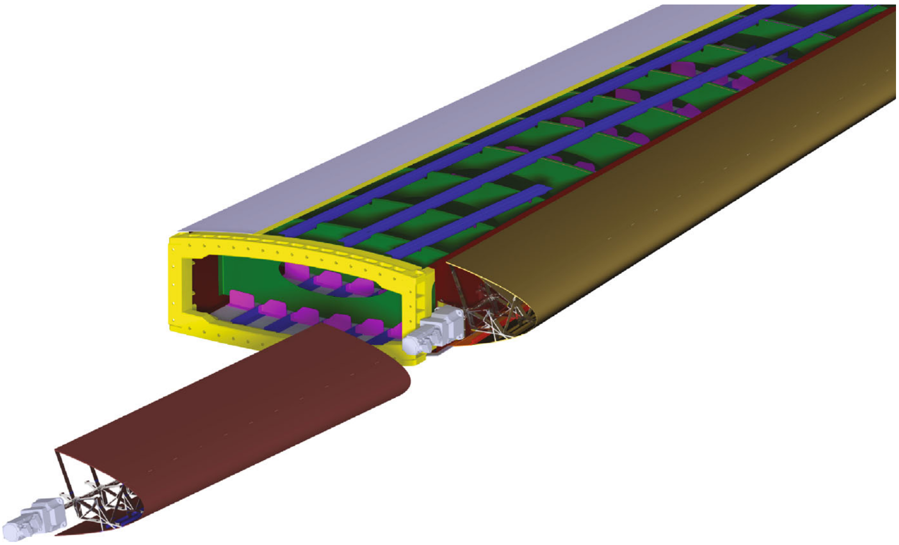

Figure 24: CAD model of the wing-box with the droop nose.

Table 6: Actuation and weight results summary.

Item	Value	Notes
Maximum torque	655 Nm	Computed with aerodynamic loads
Actuators weight	24 kg	Two rotary actuators, one linear actuator
Droop nose weight per length	11 kg/m (inboard) 9.2 kg/m (outboard)	Kinematic chain and compliant skin included; actuators and sensor system not included

The conducted bird impact study proves that the leading-edge morphing structure is characterized by a poor impact response, due to the fact that the skin is very thin and there is also a limited number of supports and stringers, particularly in the regions where a significant morphing shape change is applied. Therefore, it is required for the airworthiness certification the implementation of mitigation measures acting to protect the spar from accidental contacts. Several solutions, such as internal hybrid protection systems that absorb, split, and deviate the impacting body [19], should be considered. To this aim, some splitters are conceived to contribute to the absorption of the impact energy. They are

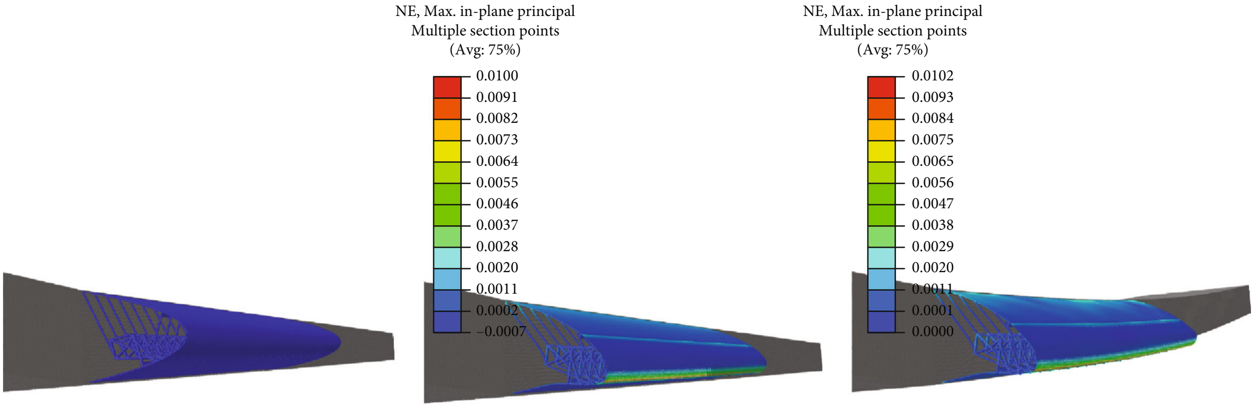

Figure 25: Assessment of the interaction between droop nose device and wing-box.

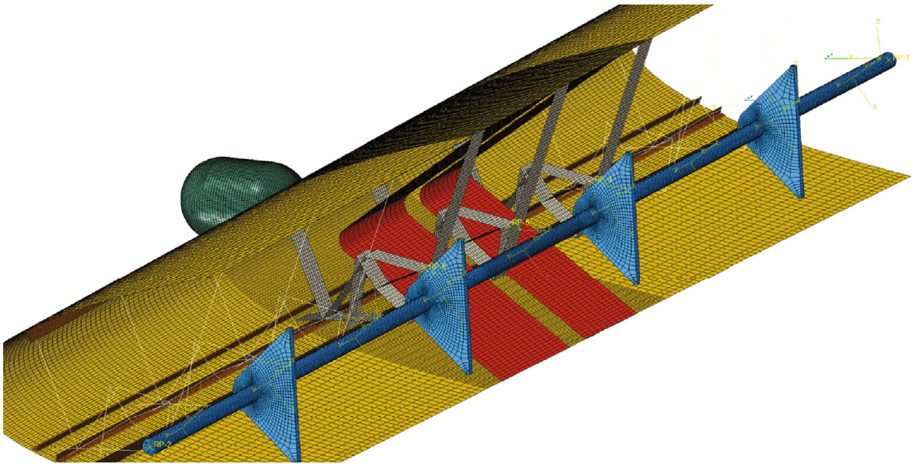

Figure 26: Testing facility for the bird impact simulation on the overall LE structure.

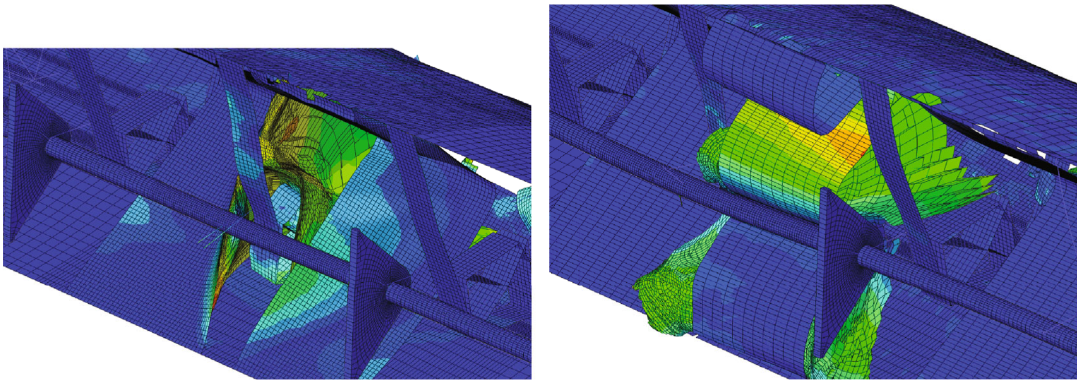

Figure 27: Bird strike test: impact on a compliant rib (left) and impact between two compliant ribs (right).

placed between each couple of consecutive compliant ribs and are modelled using 2D elements. The model for the numerical simulation including the splitters and the impacting bird is represented in Figure 26.

Two different analyses are performed. The first analysis considers the bird impacting on a compliant rib, while the other analysis assumes the bird impacting between two compliant ribs.

The two cases are illustrated in Figure 27. In the first scenario, the numerical simulation shows that the bird penetrates the skin structure, the splitters near at the impact region absorbs part of the bird energy and then the compliant rib absorbs the impact energy without fractures. In the second scenario, the skin cannot still absorb the impact energy. The splitter deforms and this time it impacts against the front spar of the wing. The splitter collapses because the bird does

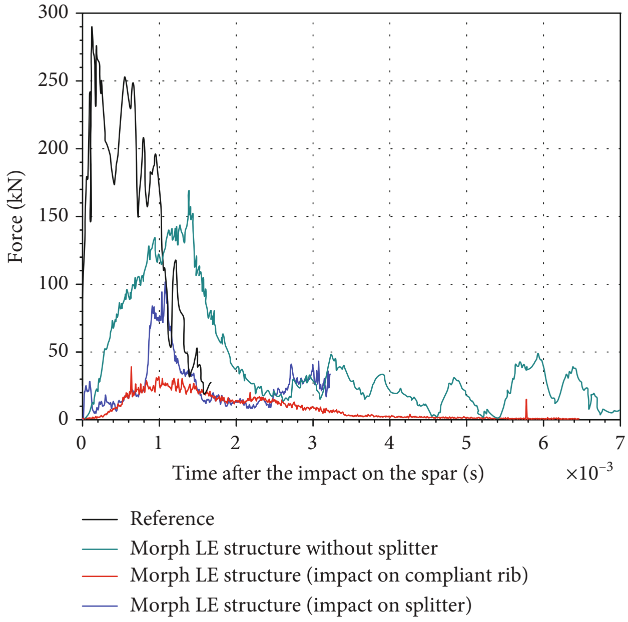

FIGURE 28: Bird strike test: reaction force on the front spar.

not impact in its centre, as instead modelled during the splitter design.

Anyway, the splitter reduces the overall reaction force on the front spar, as depicted in Figure 28. The reduction with respect to the situation without splitters is of the 75% if the impact is on a compliant rib, and it is of the 40% if the impact is between two ribs. Therefore, the introduction of splitters is essential to guarantee the bird impact requirement.

7. Conclusions

This paper describes the advanced design phase of a morphing droop nose device to be installed on a 90 passengers regional aircraft, in the framework of the Clean Sky 2 Airgreen project. The design starts from the preliminary results obtained for the optimal aerodynamic shape and the topology solution of the internal structure.

The detailed design is conducted with the aim to achieve the requested performance, while satisfying all the requirements for the device under analysis. A special effort is devoted to guarantee the structural feasibility of the conceived solution in terms of strength assessment. The structural design phase includes considerations about the accessibility of the device, foreseeing the presence of a removable inspection panel.

Verification on a medium-fidelity model of the complete device is performed, followed by detailed analyses on higher fidelity models of the internal structure. The results confirm the validity of the solution obtained by means of the proposed optimization procedures.

After that, starting from the finite element models, a complete corresponding CAD model is realized. At this phase, the assembly of the various components of the device is modelled in detail, including the actuators and the kinematic chain conceived to accomplish the morphing shape change. Regarding the actuation system, studies on the required power are conducted, leading to the selection of the suitable actuators, also considering the occupied space for the installation. Moreover, weight estimation is presented.

Finally, other important verifications are reported. A static assessment validates the interaction between the designed device and the structural wing-box. Bird strikes analyses are conducted in various cases to ensure the safety of the leading-edge device according to the certification rules, showing the need for an appropriate support structure to absorb the impact energy.

The results reported here demonstrate the high TRL achieved by the DN morphing project and show how the solution adopted is ready for experimental validation. A 1 : 3 scale test will be conducted by 2020 within the same project on a wind tunnel test model. After this activity, it is possible to imagine a full-scale test of a prototype developed for the final evaluation phase.

Data Availability

All the data supporting the results were shown in the paper and can be applied from the corresponding author.

Conflicts of Interest

The authors declare that there is no conflict of interest regarding the publication of this paper.

Acknowledgments

Special thanks go to Alessandro Airoldi, Alessandro Gilardelli, and Chiara Mirani for their contribution to the bird strike simulations. The AirGreen2 Project has received funding from the Clean Sky 2 Joint Undertaking, under the European's Union Horizon 2020 research and innovation Programme, under grant agreement no 807089–REG GAM 2018–H2020-IBA-CS2-GAMS-2017.

References

[1] S. Barbarino, O. Bilgen, R. M. Ajaj, M. I. Friswell, and D. J. Inman, “A review of morphing aircraft,” *Journal of Intelligent Material Systems and Structures*, vol. 22, no. 9, pp. 823–877, 2011.

[2] A. De Gaspari, L. Riccobene, and S. Ricci, “Design, Manufacturing and Wind Tunnel Test of a Morphing Wing Based on Compliant Structures,” in *24th AIAA/AHS Adaptive Structures Conference*, pp. 307–324, Curran Associates, Red Hook, NY, San Diego, California, USA, 2016.

[3] J. Cooper, A. Suleman, S. Ricci et al., “SMorph—Smart Aircraft Morphing Technologies Project,” in *51st AIAA/ASME/ASCE/AHS/ASC Structures, Structural Dynamics, and Materials Conference*, pp. 1–14, Orlando, Florida, 2010.

[4] G. Diodati, A. Concilio, S. Ricci et al., “Estimated performances of an adaptive trailing edge device aimed at reducing fuel consumption on a medium–size aircraft,” in *Industrial and Commercial Applications of Smart Structures Technologies 2013*, pp. 1–16, San Diego, CA, USA, 29 March 2013.

[5] A. De Gaspari and S. Ricci, "A Two-Level approach for the optimal design of morphing wings based on compliant structures," *Journal of Intelligent Material Systems and Structures*, vol. 22, no. 10, pp. 1091–1111, 2011.

[6] S. Kota, R. Osborn, G. Ervin, D. Maric, P. Flick, and D. Paul, "Mission Adaptive Compliant Wing: Design, Performance and Flight Test Results," in *50th AIAA/ASME/ASCE/AHS/ASC Structures, Structural Dynamics, and Materials Conference*, Evora, Portugal, 4 May 2009.

[7] A. De Gaspari, A. Gilardelli, S. Ricci, and A. Airoldi, "Design of a Leading Edge Morphing Based on Compliant Structures for a Twin–Prop Regional Aircraft," in *2018 AIAA/AHS Adaptive Structures Conference*, Kissimmee, Florida, 8 Jan 2018.

[8] F. Rea, F. Amoroso, R. Pecora, and F. Moens, "Exploitation of a Multifunctional Twistable Wing Trailing–Edge for Performance Improvement of a Turboprop 90–Seats Regional Aircraft," *Aerospace*, vol. 5, no. 4, 2018.

[9] F. Moens, "Augmented Aircraft Performance with the Use of Morphing Technology for a Turboprop Regional Aircraft Wing," *Biomimetics*, vol. 4, no. 3, 2019.

[10] A. De Gaspari and S. Ricci, "Knowledge-based shape optimization of morphing wing for more efficient aircraft," *International Journal of Aerospace Engineering*, vol. 2015, Article ID 325724, 19 pages, 2015.

[11] M. Drela, "A User's Guide to MSES 3.05," *MIT - Department of Aeronautics and Astronautics*, 2007, http://web.mit.edu/drela/Public/web/mses/mses.pdf.

[12] L. Cambier, S. Heib, and S. Plot, "The OneraelsACFD software: input from research and feedback from industry," *Mechanics & Industry*, vol. 14, no. 3, pp. 159–174, 2013.

[13] A. De Gaspari and F. Moens, "Aerodynamic shape design and validation of an advanced high-lift device for a regional aircraft with morphing droop nose," *International Journal of Aerospace Engineering*, vol. 2019, Article ID 7982168, 21 pages, 2019.

[14] K. Deb, *Multi-Objective Optimization Using Evolutionary Algorithms*, Wiley, 2005.

[15] "Simulia, "Abaqus Analysis User's guide," Simulia Help".

[16] S. Vasista, J. Riemenschneider, B. van de Kamp et al., "Evaluation of a compliant droop-nose morphing wing tip via experimental tests," *Journal of Aircraft*, vol. 54, no. 2, pp. 519–534, 2017.

[17] EASA European Aviation Safety Agency, "Certification Specifications and Acceptable Means of Compliance for Large Aeroplanes CS-25," Amendment 20, 24 August 2017.

[18] "Simulia, "A Strategy for Bird Strike Simulations using Abaqus/Explicit," Simulia Help".

[19] C. Chary, "Development and validation of a bird strike protection system for an enhanced adaptive droop nose," in *Smart Intelligent Aircraft Structures (SARISTU)*, M. Papadopoulos, Ed., pp. 71–83, Springer, Cham, 2016.